

Investigating the Morphological Evolution, Electron Paramagnetic Resonance, & Electrical Properties of Barium Titanate with Sn-Incorporation



Sachin Kumar, Anurag Pritam, Vaibhav Shrivastava, O. P. Thakur, and Vandna Luthra

1 Introduction

Researchers widely use barium titanate (BT) based perovskite ceramics for their dielectric properties, structural stability, and environmentally friendly nature [1, 2]. The highest value of BT's dielectric constant is typically found near its Curie temperature, which is approximately ca. 120 °C [3]. Many modern applications such as MLCCs (Multi-layer ceramic capacitors), and FeRAM (Ferroelectric Random Access Memory) require a high dielectric constant over a broad temperature range. Some researchers have utilized tin (Sn) to lower the transition temperature and achieve high dielectric constant near RT. [4, 5] The ionic radius of tin in its 6-coordinate state is larger than that of titanium ($R_{\text{Sn}} (69.0 \text{ pm}) > R_{\text{Ti}} (60.5 \text{ pm})$) [6]. As a result, tin occupies more void space at B-site than the titanium ions, causing the decrease of structural transition temperature from tetragonal to cubic [7].

Sn-incorporated BT ($\text{Ba}(\text{Ti}_{1-z}\text{Sn}_z)\text{O}_3$) is a binary solid solution composed of non-ferroelectric BaSnO_3 ($T_c = -260 \text{ }^\circ\text{C}$) and ferroelectric BaTiO_3 ($T_c = 120 \text{ }^\circ\text{C}$). The transition temperature of the solid solution can be controlled by varying their concentrations [8]. Besides, the properties of Sn-incorporated BT are expected to

S. Kumar (✉)

Department of Physics & Astrophysics, University of Delhi, Delhi 110007, India
e-mail: sachscientist@gmail.com

S. Kumar · V. Luthra

Department of Physics, Gargi College, Siri Fort Road, New Delhi 110049, India

A. Pritam · V. Shrivastava

Department of Physics, Shiv Nadar University, G.B. Nagar, Greater Noida 201314, India

O. P. Thakur

Solid State Physics Laboratory, Timarpur, Delhi 110054, India

be tuned by the composition and the processing conditions [9]. Wei et al. (2011) incorporated tin at B-site in BT and optimized the sintering temperature for the whole series from 0 to 100 mol% incorporation. It has been reported that a higher sintering temperature or soaking time is required for tin incorporation at the B-site with an increase in tin doping due to its relatively large ionic radius and mass as compared to native titanium ion. Horchidan et al. observed the highest value of dielectric constant ($\sim 10,000$) for 10 mol% tin-doped sample, sintered at 1300 °C for 4 h [7]. Kalyani et al. synthesized different compositions of tin-doped BT using two-step sintering and studied the variation in phase transition temperatures [10]. Nath et al. investigated the variation in the density of tin-doped BT samples with varying sintering temperatures from 1150 to 1400 °C and an increase in the density was observed with an increase in sintering temperature [11]. Wang et al. synthesized compositions of tin and zirconium doping in BT ($\text{Ba}(\text{Ti}_{0.94}\text{Sn}_{0.06-x}\text{Zr}_x)\text{O}_3$ for $0.00 \leq x \leq 0.06$) at sintering temperature from 1450 to 1550 °C [4]. It has been observed that higher soaking time or sintering temperature is required for tin incorporation at the B-site with an increase in tin doping [12].

Different sintering temperatures and soaking times have been used to optimize the dielectric properties for several tin doping compositions but there is a lack of discussion over the centralized idea of morphological development and corresponding defect concentration. Therefore, the present work emphasizes on these areas along with other structural and ferroelectric investigations. The EPR has been used to understand the nature of defects and to the best of our knowledge has rarely been investigated for this system. Such investigations provide insights into the process of material formation and develop an understanding of the structure–property relationship.

2 Experimental Technique

The present study involved synthesizing tin-doped BT powders using a solid-state ceramic route, with the formula $\text{BaTi}_{1-z}\text{Sn}_z\text{O}_3$; $z = 0, 0.02, 0.05, 0.07, \text{ and } 0.1$. The samples were given labels BT, BTS2, BTS5, BTS7, and BTS10, respectively. The synthesis process involved mixing barium carbonate (Sigma-Aldrich, 99.9% purity), titanium oxide (Merck, > 99% purity), and stannic oxide (Loba Chemie, 99.8% purity) in the required stoichiometric proportions. The mixture was then milled for 24 h using a horizontal bar roller ball mill with IPA. The resulting suspension was subsequently dried for 8 h at 100 °C and then calcined at 1200 °C for 3 h.

The pellets were then pressed using a uniaxial pellet-pressing machine after grinding the powders with 2% by weight Poly Vinyl Alcohol. Subsequently, the pellets were sintered at 1300 °C for 3 h. The XRD patterns were obtained using a Rigaku Ultima-IV X-ray diffractometer, $\text{Cu-K}\alpha$ radiation of 1.5418 Å. The lattice parameters were determined through Rietveld refinement. The strain and crystallite sizes were calculated using Williamson Hall plots. The SEM micrographs were obtained from the fractured portions of the pellets on a Jeol-JSM 6610LV, and the particle size was measured using imageJ software. Furthermore, the sintered powder

was subjected to room temperature (RT) EPR study using a Bruker EMX EPR spectrometer. The Lande's g -factor for a specific resonance peak was calculated using the formula.

$$g = \frac{h \cdot \nu_0}{\mu_B \cdot H} \quad (1)$$

where h is Planck's constant, ν_0 is the operating frequency (9.876 GHz), μ_B and H are Bohr Magneton (9.274×10^{-24} J/T) and the corresponding applied magnetic field. The dielectric measurements were taken on these samples in the temperature range from RT to 300 °C. The PM-300 piezo-meter was used to measure the piezoelectric charge coefficient (d_{33}) of the samples after they were polled at room temperature for 30 min with 15 kV/cm. Polling aligns the ferroelectric domain in the direction of the applied electric field. Thereafter, domains give a collective response, whereas, in an unpolled sample randomly oriented domains generate random electric fields on applying pressure and as a result, a very low d_{33} value is obtained. The P-E hysteresis loops were obtained at RT using a hysteresis loop tracer based on a modified Sawyer and Tower circuit provided by M/s Marine India Pvt. Ltd. in Delhi.

3 Results and Discussion

3.1 X-Ray Diffraction

The X-ray diffraction (XRD) patterns in Fig. 1. revealed that the samples had a tetragonal phase formation conforming to JCPDS #83–1875 [3]. A small carbonate peak at approximately 28°, was observed only in the BTS10 sample [13]. Furthermore, an observable shift toward lower 2θ values was noticed with an increase in the tin doping concentration, for all the peaks corresponding to different planes. The peak position of (110) peak has been mentioned below to quantify this effect (Fig. 1ii, Table 1). Lattice strain and crystallite size of these samples are also mentioned in Table 1. The given samples showed an increase in crystallite size with an increase in tin doping concentration. Tin substitution expands the lattice structure and its influence can also be noticed in the increase in the value of lattice volume (Table 1) [5].

As shown in Fig. 1iii, an increase in tin doping level resulted in a decrease in the splitting of (002) and (200) peaks at approximately 45°. The peak situated at a lower 2θ value indicates the longer c lattice parameter, whereas the shorter a and b parameters generate a peak at a higher 2θ value. Furthermore, the decrease in average tetragonality was found to be associated with a decrease in the c/a ratio (Table 1) [7].

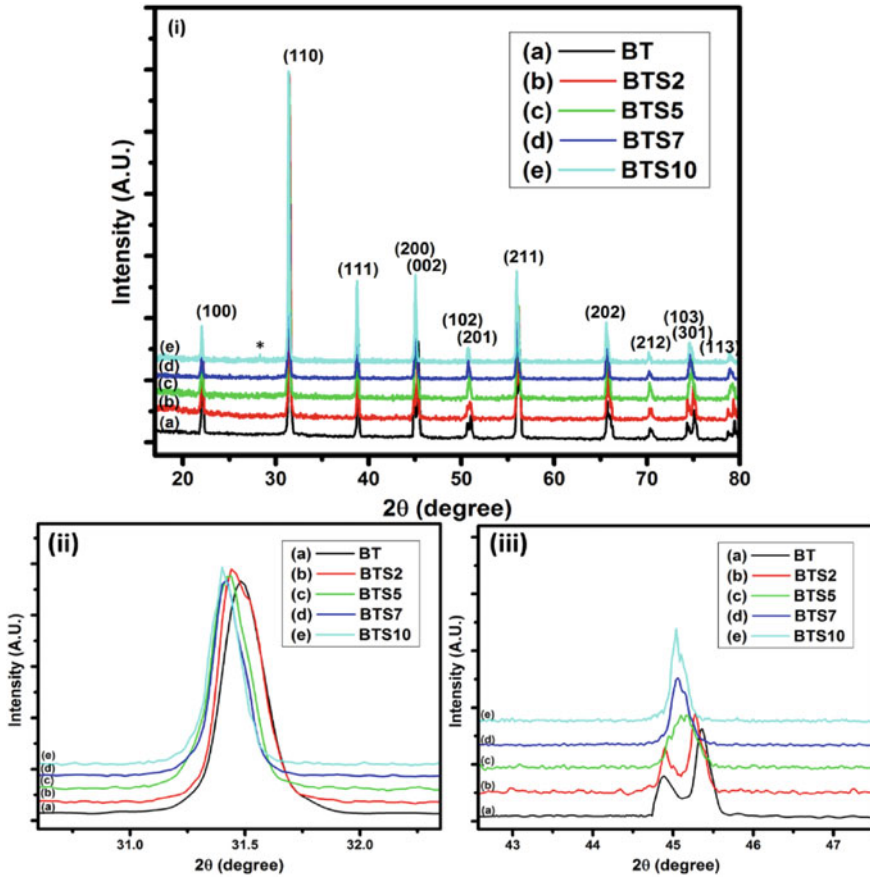


Fig. 1 i X-ray diffraction patterns of tin-doped BT ($\text{BaTi}_{1-z}\text{Sn}_z\text{O}_3$) ii An enlarged plot of the (110) peak iii An enlarged plot of the splitting of (200) and (002) peaks ca. 45°

3.2 Scanning Electron Microscopy (SEM)

The SEM micrographs of tin-doped BT samples were taken from the fractal portions of the sintered pellets (Fig. 2). The intra-granular breaking instead of inter-granular breaking was usually observed while capturing the SEM images for ≤ 5 mol% tin doping. Therefore, many fractal portions were investigated to obtain SEM images of grains with clear boundaries. Nath et al. have also shown the SEM micrographs with intra-granular breaking for tin-doped barium titanate samples [11]. The intra-granular breaking, as well as the grains with clear boundaries, are visible in Fig. 2ii.

Figure 2i shows the SEM micrograph of the undoped BT, whose average grain size was ca. $6 \mu\text{m}$. Figure 2ii and iii show the microstructure of BTS2 and BTS5 having an average grain size of ca. 16 and ca. $58 \mu\text{m}$, respectively. An increase in the grain size with the tin doping to a certain level has been noticed by researchers [14].

Table 1 The (110) peak position, lattice strain, crystallite size, lattice parameters, volume, and *c/a* ratio of the samples under investigation

Sr. no	Sample	(110) Peak position	Lattice Strain	Crystallite size (nm)	Lattice parameter, a or b (Å)	Lattice parameter, c (Å)	Lattice volume (Å ³)	<i>c/a</i>
1	BT	31.46	2.91×10^{-3}	52.34	3.9934	4.0301	64.2690	1.0092
2	BTS2	31.44	3.19×10^{-3}	56.64	3.9990	4.0300	64.4470	1.0077
3	BTS5	31.43	3.88×10^{-3}	67.68	4.0045	4.0202	64.4682	1.0039
4	BTS7	31.42	5.82×10^{-3}	99.83	4.0131	4.0177	64.7041	1.0012
5	BTS10	31.40	5.31×10^{-3}	92.51	4.0148	4.0187	64.7756	1.0010

This can be attributed to the liquid phase formed due to the isovalent substitution of tin for titanium which forms a eutectic in BaTiO₃ and BaSnO₃ systems [15, 16].

The SEM micrographs of BTS7 are shown in Fig. 3. at different magnifications. These figures provide information about the formation process of bigger particles by the combination of smaller grains. In the case of synthesis via a solid-state method, the grain size depends upon the sintering temperature [4], sintering time [17], and diffusion length[18] of the contributing ions at that temperature. In Fig. 3i, the micrograph was taken at a lower magnification to get a broader view of surface morphology. It can be observed from the morphology (Fig. 3i) that the small grains are fusing among each other to form a bigger particle. The representative white lines are marked along the tentative grain boundary. Figure 3ii is a higher magnification of the same morphology at the position of that white line rectangular box as shown in Fig. 3i. Figure 3ii shows the micrograph of these grain boundaries. Furthermore, in Fig. 3iii the image at even higher magnification shows that the small grains are 0.96 μm in size. The basic difference between the accumulation and the grain boundary is that the grains across the boundary are not diffusing into each other.

3.3 Electron Paramagnetic Resonance (EPR)

The EPR patterns of the undoped and tin-doped barium titanate samples are given in Fig. 4. The EPR signals corresponding to barium and titanium vacancies are observed at $g = 1.974$ and $g = 2.004$, respectively [19, 20]. The undoped BT showed a minor bump dedicated to barium vacancies at $g = 1.974$. In the case of tin-doped samples, an intense barium vacancy peak was observed for BTS2 and its intensity reduced with an increase in tin doping concentration. Barium vacancies are shallow defects at the grain surface [21]. While the signal for titanium vacancy at $g = 2.004$ was

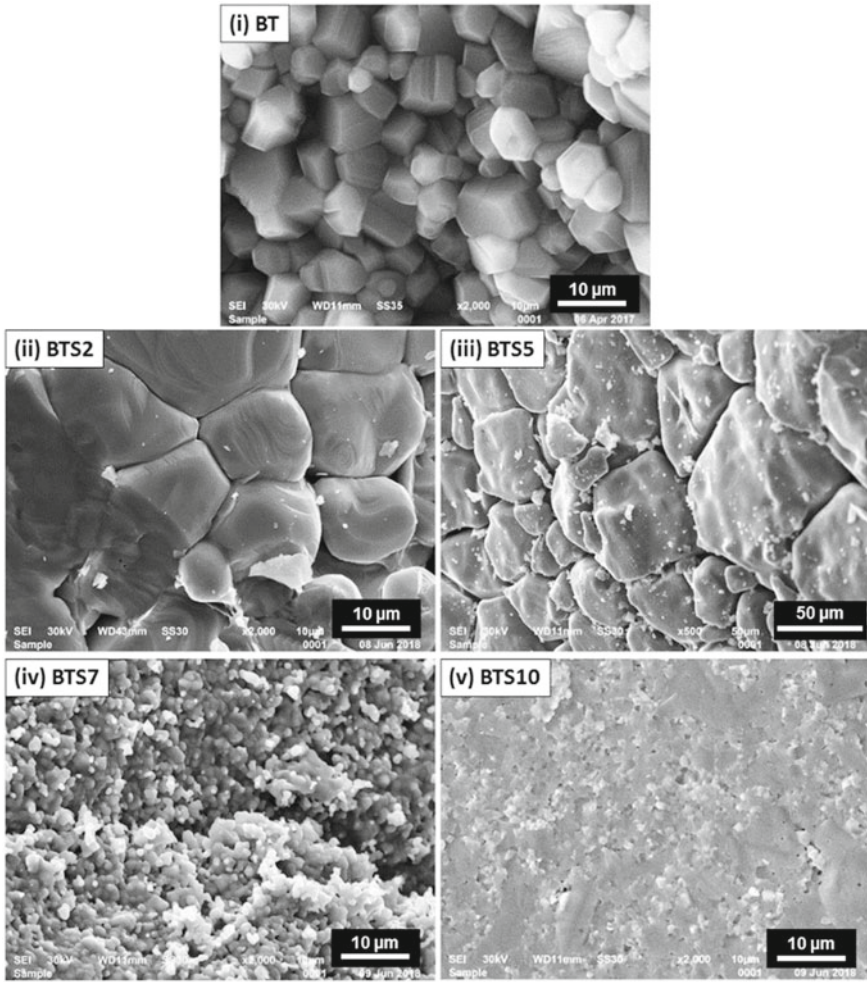


Fig. 2 SEM images of i BT ii BTS2 iii BTS5 iv BTS7 v BTS10 samples

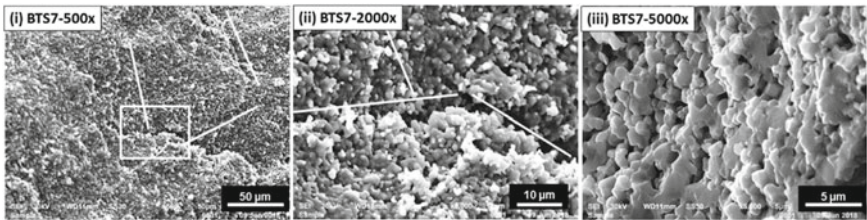
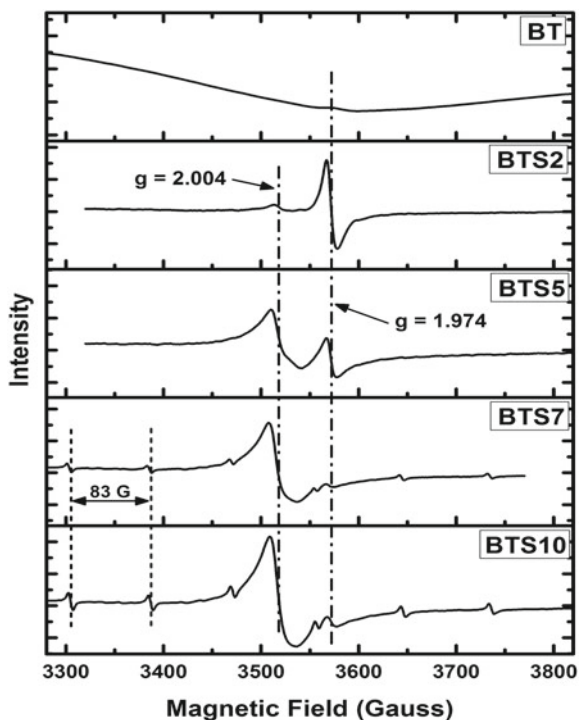


Fig. 3 SEM images of BTS7 at i 500, ii 2000, and iii 5000 magnifications

found to increase with the increase in tin doping concentration. The increase in the number of defects like B-site vacancy could be attributed to the fact that tin is a relatively heavier element than titanium and tin ions were not able to diffuse up to the required length and occupy all the stoichiometrically available titanium sites. Therefore, the intensity of titanium vacancy peak increases with an increase in tin-doping concentration. The partial substitution of tin at B-site in barium titanate has also been addressed by Veselivonic et al. by Rietveld refinement of the XRD data and XRF (X-ray Fluorescence) spectroscopy [8].

A group of 6 equidistant peaks (sextet) can also be seen emerging with increasing doping concentration because of the increase in cubic nature in the system [22, 23]. This has been reported in the literature as the hyperfine structure of Manganese ion [22]. In the present study, the separation between the consequent peaks in the present work is close to 83 Gauss. This confirms that the observed peaks are because of the presence of Mn^{2+} ions in the sample having a spin of $5/2$ [23].

Fig. 4 The EPR data of undoped and tin-doped barium titanate samples



3.4 Dielectric Properties

Figure 5i shows the plots of dielectric constant with respect to temperature at 1 kHz frequency. Figure 5ii and iii represent the dielectric constant vs temperature curves of BTS2 and BTS10 samples at different frequencies.

A composition-dependent variation in T_c and dielectric constant is observed. The maximum value of the dielectric constant has been observed for BTS2 at a transition temperature of 106 °C. The values of the T_c and the respective dielectric constants are shown in Table 2 for various samples. It has been noticed from the XRD pattern that Sn incorporation decreases the average tetragonality of the material (Fig. 1iii).

This infers a decrease in the polarization density of the material with tin doping, which is contrary to the enhancement in its dielectric constant. Shi et al. have investigated the enhancement of dielectric constant in BT because of tin incorporation and

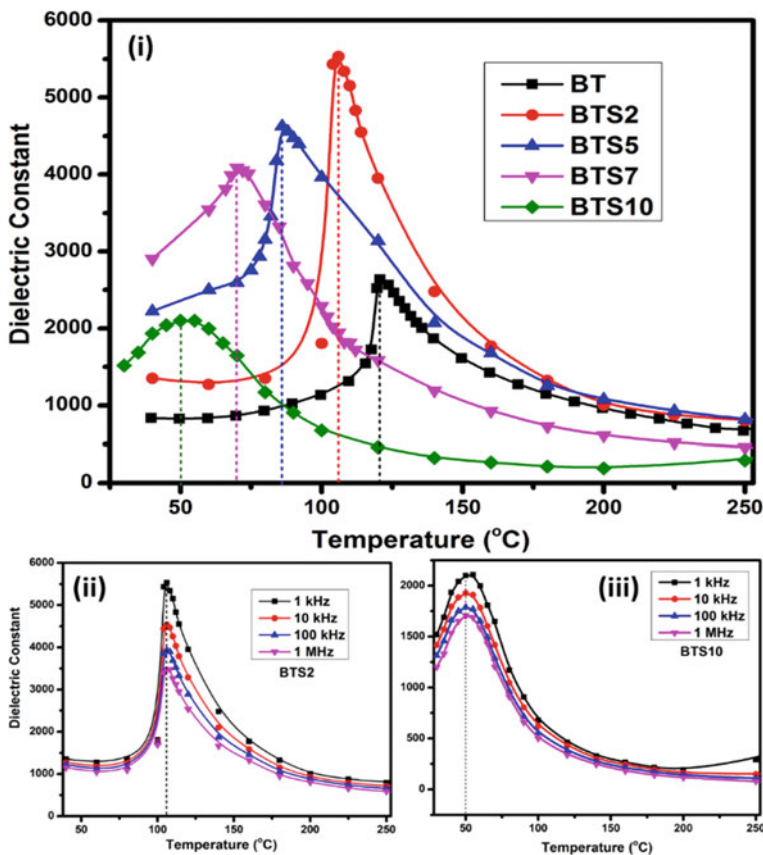


Fig. 5 i Dielectric constant with respect to temperature for different doping concentrations ii dielectric constant vs. temperature curves for BTS2 and iii BTS10 at different frequencies

Table 2 The values of the transition temperature, dielectric constant at 40 °C and T_c (1 kHz), and diffusivity coefficient of the samples under investigation

Sr. no	Sample name	Transition temperature (T_c) (°C)	Dielectric const. at 40 °C (1 kHz)	Dielectric const. at T_c (1 kHz)	(γ) Diffusivity coefficient
1	BT	120	837	2637	1.083 ± 0.009
2	BTS2	106	1352	5533	1.187 ± 0.019
3	BTS5	86	2224	4625	1.230 ± 0.014
4	BTS7	70	2903	4086	1.342 ± 0.016
5	BTS10	50	1934	2099	1.807 ± 0.048

it was observed that besides the increase in an average symmetry, tin doping distorts the lattice structure and increases the local polarization forming polar regions [24]. Therefore, the increase in the dielectric constant of BTS2 could be attributed to doping-induced structural distortions. The extent of the enhancement in local polarization with tin doping is a temperature-dependent process as it can be generalized from the literature that different tin doping compositions show their optimum values of dielectric constant for different sintering temperatures [19, 25, 26]. The maximum value of dielectric constant was observed for 2 mol% tin-doping levels when the samples were sintered at 1300 °C.

For doping concentrations above 2 mol%, the decrease in tetragonality becomes more significant than local polarization, causing the dielectric constant to decrease at its transition temperature. The sample BTS7 demonstrated the highest value of dielectric constant near room temperature (at 40 °C) due to its transition temperature being closer to room temperature, combined with an optimal sintering temperature.

The data was analyzed using the Modified Curie–Weiss Law [26]. A gradual increase in diffusivity from BT ($\gamma = 1.08$) to BTS7 ($\gamma = 1.34$) was observed, but its value increases high for BTS10 samples ($\gamma = 1.80$). This sample also showed a low dielectric constant. With the increase in tin content, the peak of the dielectric permittivity becomes progressively more diffused (BTS10), but the peak position doesn't change (Fig. 5iii). Therefore, the high value of diffusivity coefficient ($\gamma = 1.80$) and broad transition in BTS10 sample (Fig. 5iii) manifests DPT (Diffuse Phase Transition) behavior [27]. The incorporation of dopant ions such as tin in the place of a native titanium ion distorts the long-range uniformity and gives rise to the increase in diffusivity [28]. The increasing number of B-site vacancy defects has also been discussed in the EPR investigation, which can also be a contributing factor to the increasing diffusivity with an increase in tin doping concentration.

3.5 P-E Hysteresis Loop

P-E hysteresis loops of the tin-doped BT samples are shown in Fig. 6. The maximum remnant polarization ($2P_r$) was observed to be $11.56 \mu\text{C}/\text{cm}^2$ for BTS2. However, the value of remnant polarization was found to decrease with an increase in tin doping. However, Horchidan et al. have observed an increase in remnant polarization up to 5 mol% tin doping in BT which decreases afterward [27]. Besides, the minimum value of coercivity was also observed for BTS2. Its value increased for BTS5 and started decreasing thereafter. It can also be noticed that the saturation polarization is also found to be the maximum for BTS2 sample (Table 3), which can be correlated with the highest value of the dielectric constant obtained for this sample.

As the tin content increased, a reduction in both the maximum and remnant polarization was observed. This can be attributed to the non-ferroelectric nature of BaSnO_3 , leading to a decrease in polarization [29]. Furthermore, increased Sn doping caused BaTiO_3 to transition to DPT and then relaxor behavior, resulting in

Fig. 6 Plots demonstrating the P-E hysteresis loops of the undoped and tin-doped BT samples

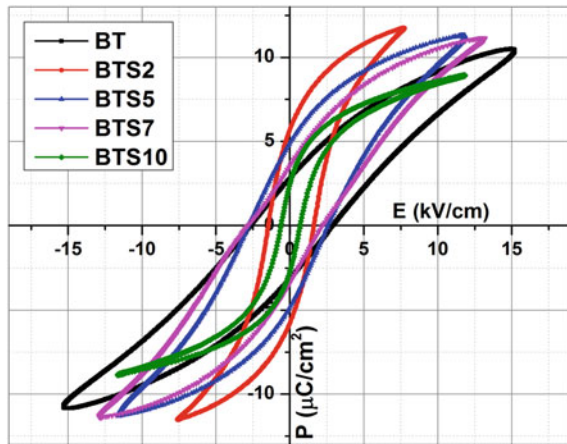


Table 3 The $2P_r$ (remanence), $2E_c$ (coercivity), P_s (saturation polarization), and piezoelectric coefficient (d_{33}) of the samples under investigation

Sr. No	Sample	($2P_r$) Remanence ($\mu\text{C}/\text{cm}^2$)	($2E_c$) Coercivity (kV/cm)	Saturation Polarization (P_s) ($\mu\text{C}/\text{cm}^2$)	d_{33} (pC/N)
1	BT	5.9	5.54	10.6	79
2	BTS2	11.56	3.08	11.64	114
3	BTS5	9.88	5.36	11.26	48
4	BTS7	7.00	5.04	11.22	26
5	BTS10	5.17	1.26	8.19	16

slender hysteresis loops with lower polarization and coercive field, values given in Table 3.

3.6 Piezoelectric Coefficient (d_{33})

The maximum value of d_{33} was observed for BTS2 sample. It decreases after 2 mol% doping because of the dominance of cubic nature. It has been stated by researchers that the switching of dipoles is more accessible and quicker if the energy barrier for polarization switching is low [30, 31]. It has also been established that the energy barrier for polarization switching decreases with an increase in tin content in BT [31]. The high value of the piezoelectric coefficient (d_{33}) can be correlated with the lower value of coercivity for BTS2 than the coercivity of its adjoining samples (Table 3). High saturation polarization from the P-E hysteresis loop (Fig. 6) and high dielectric constant observed for BTS2 sample suggest the existence of enhanced polarization for this composition and could be a reason for its high piezoelectric coefficient.

4 Conclusion

The tetragonal structure of these samples was confirmed using XRD. Moreover, in SEM micrographs the particle size increased till 5 mol% tin-doping and small grain microstructure forming big accumulations was observed for 7 mol% tin doping. EPR data exhibited an increase in titanium vacancies with tin doping because of the diffusion-limited substitution process. The intensity of Mn^{2+} hyperfine peaks was also found to increase with an increase in tin doping. The diffusion-limited substitution can be supported by the increase in vacancy defects with the increase in tin doping concentration. The BTS2 sample showed the highest value of the dielectric constant at its transition temperature because of an increase in polarization initiated by doping-induced distortions. It is also evident from the P-E hysteresis loop of BTS2 showing the highest value of saturation (P_s), remnant polarization ($2P_r$) and the lowest value of coercive field ($2E_c$). Tin-doped samples achieved their saturation polarization at a lower electric field than undoped BT because of the decrease in domain switching energy. The piezoelectric coefficient (d_{33}) of BTS2 was also found to be the maximum because of faster domain switching and enhanced polarization.

Acknowledgements We are thankful to Star College Grant, Gargi College-wide SAN/No.102/IFD/DBT/SAN/1911/2008-09 (Department of Biotechnology). We are thankful to Principal, Gargi College and USIC instrumentation facility, University of Delhi for providing various facilities.

References

1. Yoon DH (2006) Tetragonality of barium titanate powder for a ceramic capacitor application. *J Ceram Process Res* 7(4):343–354
2. Chen WP, Shen ZJ, Guo SS, Zhu K, Qi JQ, Wang Y, Chan HLW (2008) A strong correlation of crystal structure and Curie point of barium titanate ceramics with Ba/Ti ratio of precursor composition. *Phys B Condens Matter* 403(4):660–663
3. Kumar S, Thakur OP, Luthra V (2018) Modulating the effect of yttrium doping on the structural and dielectric properties of Barium titanate. *Phys Status Solidi A* 215(7):1700710
4. Wang N, Zhang BP, Ma J, Zhao L, Pei J (2017) Phase structure and electrical properties of Sn and Zr modified BaTiO₃ lead-free ceramics. *Ceram Int* 43(1):641–649
5. Wei X, Yao X (2007) Preparation, structure and dielectric property of barium stannate titanate ceramics. *Mater Sci Eng B* 137(1–3):184–188
6. Dean JA (1999) Lange's Handbook of chemistry, 15th ed. McGraw Hills
7. Horchidan N, Ianculescu AC, Curecheriu LP, Tudorache F, Musteata V, Stoleriu S, Dragan N, Crisan D, Tascu S, Mitoseriu L (2011) Preparation and characterization of barium titanate stannate solid solutions. *J Alloys Compd* 509(14):4731–4737
8. Veselinović, L., Mitrić, M., Mančić, L., Vukomanović, M., Hadžić, B., Marković, S., Uskoković, D (2014) The effect of Sn for Ti substitution on the average and local crystal structure of BaTi_{1-x}Sn_xO₃ (0 ≤ x ≤ 0.20). *J Appl Crystallogr* 47(3):999–1007
9. Cai W, Fan Y, Gao J, Fu C, Deng X (2011) Microstructure, dielectric properties and diffuse phase transition of barium stannate titanate ceramics. *J Mater Sci* 22(3):265–272
10. Kalyani AK, Brajesh K, Senyshyn A, Ranjan R, Kalyani AK, Brajesh K, Senyshyn A, Ranjan R (2016) Orthorhombic-tetragonal phase coexistence and enhanced piezo-response at room temperature in Zr, Sn, and Hf modified BaTiO₃. *Appl Phys Lett* 252906(2014):1–5
11. Nath AK, Medhi N (2012) Density variation and piezoelectric properties of Ba(Ti_{1-x}Sn_x)O₃ ceramics prepared from nanocrystalline powders. *Bull Mater Sci* 35(5):847–852
12. Lu DY, Guan DX (2017) Photoluminescence associated with the site occupations of Ho³⁺ ions in BaTiO₃. *Sci Rep* 7(1):1–8
13. Ashiri R (2016) RSC Advances nanocrystals from mechanically activated BaCO₃ and TiO₂ powders : innovative mechanochemical. *RSC Adv* 6(21):17138–17150
14. Ansaree MJ, Upadhyay S (2017) Study of phase evolution and dielectric properties of Sn-doped barium titanate. *Emerg. Mater. Res.* 1817(4):21–28
15. Bilous A, V'yunov O, Kovalenko L (2001) (Ba, Y)(Ti, Zr, Sn)O₃-based PTCR materials. *Ferroelectrics* 254(1–4):91–99
16. Matsuo Y, Sasaki H (2019) Exaggerated grain growth in Liquid-Phase sintering of BaTiO₃. *J. Am. Ceram. Soc. Notes.* 12:471
17. Bongkarn T, Wattanawikkam C (2009) The preparation of Ba(Sn_{0.1}Ti_{0.9})O₃ ceramics via a solid state reaction method. *Ferroelectrics* 382(1):56–61
18. Miao S, Pokorny J, Pasha UM, Thakur OP, Sinclair DC, Reaney IM (2009) Polar order and diffuse scatter in Ba(Ti_{1-x}Zr_x)O₃ ceramics. *J Appl Phys* 106(11):1–6
19. Dunbar TD, Warren WL, Tuttle BA, Randall CA, Tsur Y (2004) Electron paramagnetic resonance investigations of Lanthanide-Doped barium titanate: dopant site occupancy. *J Phys Chem B* 108(3):908–917
20. Kolodiaznyi T, Petric A (2003) Analysis of point defects in polycrystalline BaTiO₃ by electron paramagnetic resonance. *J Phys Chem Solids* 64(6):953–960
21. Lu DY, Sun XY, Toda M (2006) Electron spin resonance investigations and compensation mechanism of europium-doped barium titanate ceramics. *Jpn J Appl Phys* 45(11):8782–8788
22. Choudhury D, Pal B, Sharma A, Bhat SV, Sarma DD (2013) Magnetization in electron-and Mn-doped SrTiO₃. *Sci Rep* 3:1–4
23. Slipenyuk AM, Glinchuk MD, Bykov IP, Yurchenko LP, Mikheev VA, Frenkel OA, Tkachenko VD, Garmash EP (2003) Study of BaTiO₃ ceramics doped with Mn and Ce or Nb and Sr. *Condens Matter Phys* 6(2):237–244

24. Shi T, Xie L, Gu L, Zhu J (2015) Why Sn doping significantly enhances the dielectric properties of $\text{Ba}(\text{Ti}_{1-x}\text{Sn}_x)\text{O}_3$. *Sci Rep* 5:8–11
25. Xiaoyong W, Yujun F, Xi Y (2003) Dielectric relaxation behavior in barium stannate titanate ferroelectric ceramics with diffused phase transition. *Appl Phys Lett* 83(10):2031–2033
26. Horchidan N, Ianculescu AC, Vasilescu CA, Deluca M, Musteata V, Ursic H, Frunza R, Malic B, Mitoseriu L (2014) Multiscale study of ferroelectric-relaxor crossover in $\text{BaSn}_x\text{Ti}_{1-x}\text{O}_3$ ceramics. *J Eur Ceram Soc* 34(15):3661–3674
27. Shvartsman VV, Kleemann W, Dec J, Xu ZK, Lu SG (2006) Diffuse phase transition in $\text{BaTi}_{1-x}\text{Sn}_x\text{O}_3$ ceramics: An intermediate state between ferroelectric and relaxor behavior. *J Appl Phys* 99(12):1–8
28. Jha PA, Jha AK (2013) Effects of yttrium substitution on structural and electrical properties of barium zirconate titanate ferroelectric ceramics. *Curr Appl Phys* 13(7):1413–1419
29. Kalyani AK, Krishnan H, Sen A, Senyshyn A, Ranjan R (2015) Polarization switching and high piezoelectric response in Sn-modified BaTiO_3 . *Phys Rev B—Condens Matter Mater Phys* 91(2):1–13
30. Zhu L, Zhang B, Zhao L, Li S, Zhou Y, Shi X, Wang N (2016) Large piezoelectric effect of $(\text{Ba}, \text{Ca})\text{TiO}_3 - x\text{Ba}(\text{Sn}, \text{Ti})\text{O}_3$ lead-free ceramics. *J Eur Ceram Soc* 36:1017–1024
31. Liu W, Wang J, Ke X, Li S (2017) Large piezoelectric performance of Sn doped BaTiO_3 ceramics deviating from quadruple point. *J Alloys Compd* 712:1–6